Effect of Y/Zr Ratio on Inclusions and Mechanical Properties of 9Cr-RAFM Steel Fabricated by Vacuum Melting

Guoxing Qiu, Dongping Zhan, Changsheng Li, Min Qi, Zhouhua Jiang, and Huishu Zhang

This study investigates the inclusions, microstructures, tensile properties, and impact toughness of reduced-activation ferritic/martensitic (RAFM) steels with different Y/Zr ratio contents. An optical microscope and a scanning electron microscope (SEM) were employed to determine the size and number of inclusions, and SEM and transmission electron microscope were employed to examine the inclusion types. The increase in Y/Zr ratio influenced the prior austenite grain size owing to the pinning effect of the inclusions. The result of this examination showed that the mechanical properties of the steel are closely related to the refinement of prior austenite grain size and as well as the fine submicron-sized inclusions. The average prior austenite grain sizes of the alloys were 14.5, 13.5, and 13.4 μm for the steels with different Y/Zr ratio contents (i.e., 1/2, 5/3, and 11/2, respectively). Moreover, the submicron-sized inclusions in the alloys achieved densities of 4.71×10^{16}, 4.49×10^{16}, and 3.84×10^{16}/m^3. The ductile-to-brittle transition temperature (DBTT) decreases when the Y/Zr ratio increases to 5/3. However, the DBTT increases when the Y/Zr ratio reaches 11/2 owing to inclusion coarsening. The RAFM steel with Y content of approximately 0.005 wt.% and Zr content of 0.002 wt.% was verified to exhibit an optimized combination of microstructures, tensile properties, and impact toughness.

1. Introduction

Reduced-activation ferritic/martensitic (RAFM) steels are the primary candidates for first wall and blanket structures of D–T fusion reactors owing to their good swelling resistance and thermophysical and thermomechanical properties (Ref 1-3). The popular solid solution and precipitation strengthening elements (i.e., niobium (Nb) and molybdenum (Mo)) are replaced with tantalum (Ta) and tungsten (W) to ensure low activation of the RAFM steel (Ref 4). To further improve the mechanical properties of RAFM steels, many studies were conducted by scientists worldwide. Their research mainly focused on two aspects: optimizing the previously obtained alloy content and adding new alloying elements. The former aspect mainly aims to optimize the content of W and Ta (Ref 5, 6). The chemical composition optimization has been exten-

sively investigated to ensure the excellent properties of RAFM steels based on research programs of the European Union, the USA, Japan, China, and India (Ref 7). In China, the RAFM steel is called CLAM (Fe-9.0Cr-1.5W-0.2V-0.15Ta-0.45Mn-0.05Si-0.1C) (Ref 8). Moreover, several low-activation elements [e.g., Si (Ref 9), Ti (Ref 10, 11), Zr (Ref 12), and Y (Ref 13, 14)] were added. The effect of Si in the range of 0.05–0.77 wt.% on microstructures, tensile properties, and impact toughness of CLAM steels was investigated by Sh. H. Chen and L. J. Rong, and the optimized content of Si is 0.22% (Ref 9). In Italy, BATMAN series containing approximately 0.1 wt.% of Ti and 50–60 ppm of B instead of Ta had been investigated by ENEA (Ref 11). The ENEA reported the mechanical properties similar to the existing RAFM steels with Ta. Korea developed an advanced reduced-activation alloy (ARAA) with Zr in 0.01 wt.% used as the structural material for test blanket module applications with helium-cooled ceramic reflector (Ref 12). Y. Li and Q. Y. Huang et al. reported that the addition of 0.2% yttrium reduces the strength of CLAM steels prior to irradiation, but the irradiation-resistant property of the steel improves (Ref 13). According to the studies on oxide dispersion-strengthened (ODS)–RAFM steels (Ref 15, 16), oxide particles (e.g., Y-Ti-O, Y-Zr-O, and Y-Al-O) have been introduced to RAFM steels to improve the mechanical properties and radiation resistance of the alloys. Recently, the effectiveness of introducing micro-sized Y_2O_3 particles to the RAFM steels through vacuum casting has been reported (Ref 17). Zhan (Ref 18) et al. prepared a 9Cr-Ti-Y-ODS steel through a direct alloying process in a vacuum induction furnace. According to the first principle of the calculation result, the binding energy of Y-Zr-O clusters was higher than that of Y-Al-O and Y-Ti-O clusters in the Fe matrix. This result indicated that the Y-Zr-O phase was easier to form and more stable than the Y-Al-O and Y-Ti-O phase because higher

Guoxing Qiu, State Key Laboratory of Rolling and Automation, Northeastern University, Shenyang 110819, China; and School of Metallurgy, Northeastern University, Shenyang 110819, China; **Dongping Zhan** and **Zhouhua Jiang**, School of Metallurgy, Northeastern University, Shenyang 110819, China; **Changsheng Li** and **Min Qi**, State Key Laboratory of Rolling and Automation, Northeastern University, Shenyang 110819, China; and **Huishu Zhang**, School of Metallurgy Engineering, Liaoning Institute of Science and Technology, Benxi 117004, China. Contact e-mail: zhandp1906@163.com.

stability of these clusters may enhance the nucleation rate, and the size of these clusters also decreased with the addition of Zr (Ref 19-22). To clarify the mechanism of oxide particle formation and to evaluate the effects of Y/Zr ratios on the inclusions and mechanical properties of 9Cr-RAFM steel in this research, three types of 9Cr-RAFM steel with different Y/Zr ratios were fabricated through vacuum casting.

2. Materials and Experiments

2.1 Materials

The investigated RAFM steels with various Y/Zr ratios were fabricated in a 25-kg vacuum inside a magnesia crucible. Pure iron, chromium (99.98 wt.% pure by weight), tungsten (99.95 wt.% pure by weight), and tantalum (99.91 wt.% pure by weight) were placed into the crucible in advance. These raw materials were melted with the protection of argon (0.04 MPa), and then the molten material was maintained at 1823 K and 20 Pa for 60 min to ensure the homogeneity of the alloy. Subsequently, Si (99.9 wt.% pure by weight), Mn (99.99 wt.% pure by weight), V (99.92 wt.% pure by weight), Zr (99.99 wt.% pure by weight), and Y (99.9 wt.% pure by weight) were sequentially added at 2-min intervals. The molten alloy was cast in argon protection at 1793 K. The chemical compositions of the steels are listed in Table 1. Based on their individual Y and Zr contents, the alloys were labeled as 1Y2Zr (1#), 5Y3Zr (2#), and 11Y2Zr (3#). With the increase in Y-mass fraction, the total oxygen in the steels decreased from 34 to 17 ppm, and nitrogen contents were approximately 32 ppm. The yields of Zr were very similar (approximately 95%). However, a remarkable difference was observed in the yields of Y. Hence, the yield increased with increasing amounts of Y. The amounts of Y added were 10, 30, and 50%.

2.2 Inclusion Statistics

First, the head and bottom of the ingots were removed to obtain dense and clean raw materials. Second, the samples were cut from the ingots, and their cross sections were polished. The planar size distribution of particles in the polished cross section of each sample was observed to count the inclusions by using an optical microscope (OM) at a magnification of 500 and the JSM-7800F scanning electron microscope (SEM) at a magnification of 1500. The OM was used to observe the inclusions with the size ($d_{A(i)}$) of more than 0.5 μm, whereas the SEM was utilized to observe the inclusions with the size ($d_{A(i)}$) of less than 0.5 μm. The diameter of each particle section, $d_{A(i)}$, was estimated similar to the diameter of a circle with the same area of the sectioned inclusion particle (Ref 23).

$$d_{A(i)} = \sqrt{\frac{4}{\pi} \cdot S_{A(i)}}, \tag{Eq 1}$$

where $S_{A(i)}$ is the cross-sectional area of each particle, measured using a semi-automatic image analyzer.

The mean spatial diameter of spherical particles ($\bar{d}_V$) can be expressed in the following equation, which was first derived by Fullman (Ref 23).

$$\bar{d}_V = \frac{\pi}{2} \cdot \bar{d}_{A(H)} = \frac{\pi}{2} \cdot \frac{n}{\sum_{i=1}^{n} (1/d_{Ai})}, \tag{Eq 2}$$

where $\bar{d}_{A(H)}$ is the harmonic mean diameter of the particle sections and n is the number of particles obtained for an observed area (A_{Tobs}).

The number of particles per unit volume was evaluated on the basis of the following relationship (Ref 23).

$$N_V = \frac{N_A}{\bar{d}_V},$$

where N_A is the number of particle sections per unit area and is defined as n/A_{Tobs}.

The volume fraction of spherical particles, f_V, is expressed as (Ref 23)

$$f_V = (\pi/6) \cdot \bar{d}_V^3 \cdot N_V.$$

The FEI Tecnai G20 transmission electron microscope (TEM) was employed to observe the inclusions with sizes less than 0.5 μm. During the TEM sample preparation, mechanical polishing was followed by twin-jet polishing with a solution of 7 vol.% perchloric acid in ethanol.

2.3 High-Temperature Confocal Scanning Laser Microscope

To evaluate the effect of inclusions on the austenitization, the VL2000DX–SVF17SP confocal scanning laser microscope (CSLM) was employed to capture high-quality images during the experiment under the inert gas atmosphere (argon, 6 N). The specimens had a gauge section of 5.0 mm in diameter and 4.0 mm in length. The difference in temperature between the top surface of the specimen and the bottom of the crucible was less than 5 K. The samples (φ5 mm × 4 mm) were heated to 1323 K, and this temperature was maintained for 10 min to observe the growth of austenite. They were captured in two frames per second during controlled heating at 5 K/s. When the samples were air-cooled to room temperature (RT), they were observed through the SEM.

2.4 Mechanical Properties

The plates were normalized at 1323 K for 30 min and then tempered at 1023 K for 90 min, followed by air cooling. The

Table 1 Chemical compositions of the steels (%)

Steel	C	Si	Mn	Cr	W	V	Ta	S	P	N	O	Zr	Y	Fe
1Y2Zr	0.10	0.05	0.46	9.1	1.49	0.22	0.15	0.002	0.0071	0.0032	0.0034	0.002	0.001	Bal.
5Y3Zr	0.11	0.05	0.45	9.2	1.50	0.22	0.14	0.002	0.0070	0.0034	0.0027	0.003	0.005	Bal.
11Y2Zr	0.10	0.06	0.44	9.1	1.49	0.22	0.15	0.003	0.0072	0.0031	0.0017	0.002	0.011	Bal.

steel microstructures were analyzed through the OM and SEM. A mixed solution of hydrochloric acid and ferric chloride was used to corrode the specimens for OM and SEM. The specimens for tensile and Charpy impact tests were spark-machined from heat-treated plates, transverse to the rolling direction. The tensile specimens had a gauge section of 5.0 mm in diameter and 25 mm in length, and tensile tests were performed with a strain rate of 2 mm/min. The tensile specimens were performed at RT, 573, 773, 823, 873, and 923 K. The standard V-notch Charpy specimens sized 10 mm × 10 mm × 55 mm were subjected to an impact test at temperatures between 143 and 298 K.

3. Results and Discussion

3.1 Inclusions in the Steel Ingots

The size distribution of micron-sized inclusions in the steel ingots is shown in Fig. 1. Most inclusions were smaller than 3 μm, and the proportion in every sample was more than 97%. The proportion of inclusions with sizes larger than 5 μm was less than 1%. With the increase in the Y/Zr ratio from 1/2 to 5/3, the percentage of inclusions with the sizes 0.5–1 μm gradually increased, whereas that of inclusions with other sizes showed a downward trend. When the Y/Zr ratio reached 11/2, only a slight decrease in percentage of inclusions sized 0.5–1 μm was observed. Noticeably, the inclusions in 5Y3Zr and 11Y2Zr alloys were smaller than that in 1Y2Zr alloy. Table 2 presents the statistical results of the mean spatial diameters ($\bar{d}_V$), the volume fraction of spherical particles (f_V), and density

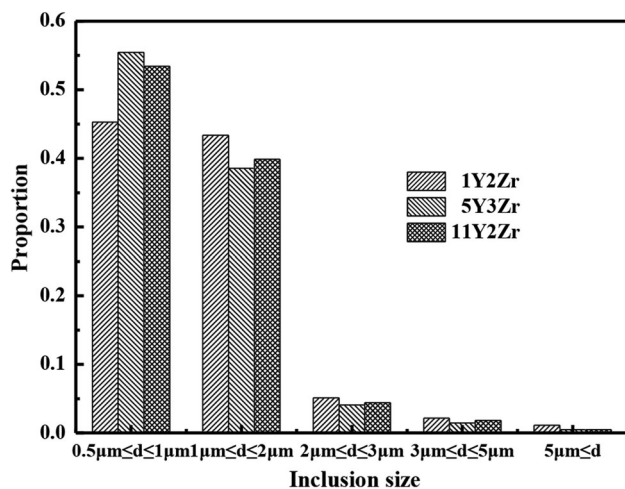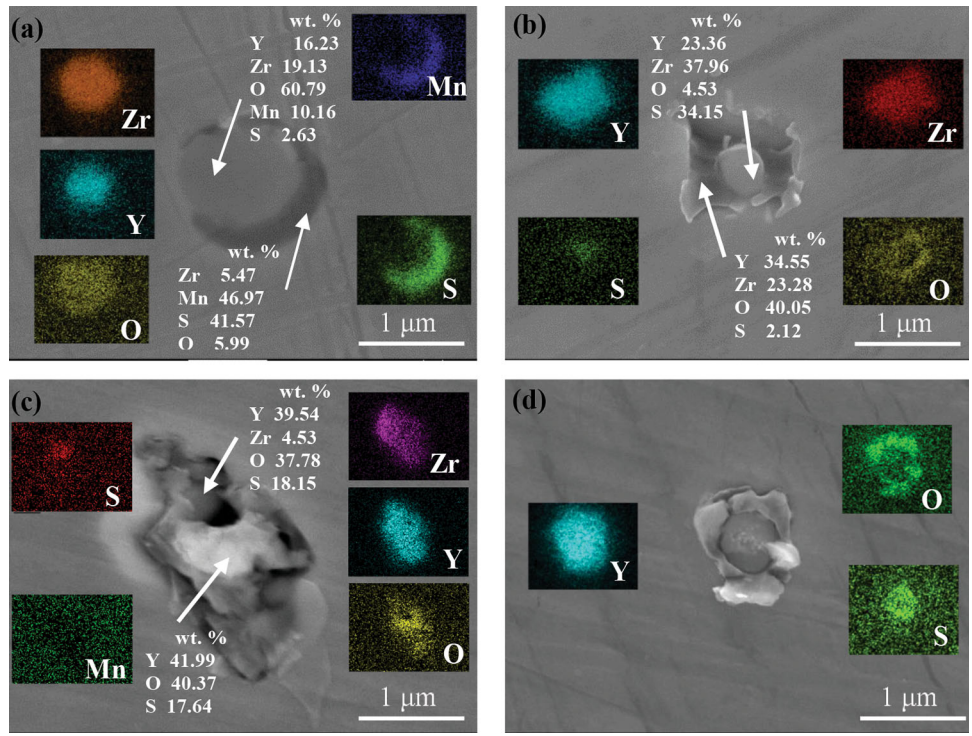**Fig. 1** Size distribution of inclusions with sizes more than 0.5 μm

(N_V) of inclusions in the ingots. With the increase in the Y/Zr ratio, the mean spatial diameters of inclusions decreased from 1.79 to 1.30 μm and then increased to 1.32 μm. Meanwhile, the density of inclusions with sizes larger than 0.5 μm increased from $1.51 \times 10^{14}/m^3$ to $2.58 \times 10^{14}/m^3$. The change of f_V presented the same rule as that of $\bar{d}_V (\geq 0.5$ μm), partially decreasing and then increasing. Regarding the density of inclusions with sizes of less than 0.5 μm, 1Y2Zr alloy has excellent performance, which is $4.71 \times 10^{16}/m^3$. 11Y2Zr alloy (3#) has the smallest value, that is, $3.81 \times 10^{16}/m^3$. The inclusions in the 9Cr steel with different Y/Zr ratios melted through vacuum casting were mainly micro-sized and sub-micrometer-sized. They were much smaller than the inclusions with Y/Y-Ti as reported by Shi and Han (Ref 17) and Wu et al. (Ref 24). The density of submicron-sized inclusions reached the reported density for the 9Cr-ODS steel prepared by Sun et al. through chemical reduction and mechanical milling (Ref 25).

When Zr and Y are added to molten steel, they combine with the oxygen and sulfur in the steel to form inclusions such as ZrO_2, Y_2O_3, YS, and Y_2O_2S. Additionally, several carbides, such as ZrC and YC_2, can be generated. Based on the data obtained from Yong (Ref 26), the standard free energies of the formation of ZrO_2, ZrC, Y_2O_3, YS, Y_2O_2S, and YC_2 at 1873 K are −347.2, −193.3, −559.3, −151.3, −516.6, and −28.3 kJ/mol, respectively. Therefore, carbides (ZrC and YC_2) are not easy to generate in molten steels. The microscale morphologies and compositions of the inclusions in the ingots are shown in Fig. 2. No pure ZrO_2 inclusions were found in the alloys. All Zr-containing inclusions contain Y. This phenomenon indicates that when Zr and Y are added to the alloys to deoxidize together, generating inclusions containing Y-Zr-O becomes easy. This finding is in accordance with the results of the first principle. Inclusions in 1Y2Zr alloy with small Y/Zr ratios were mainly Y-Zr-Mn-O-S covered by Zr-Mn-S (Fig. 2a). When the Y/Zr ratio increases, the MnS inclusion in the alloys disappears. The inclusions were mainly Y-Zr-O-S (Fig. 2b) in 5Y3Zr alloy. In the 11Y2Zr alloy with the high Y/Zr ratio, pure Y-O-S inclusions (Fig. 2d) without Zr were found. The inclusions with Zr were mainly Y-Zr-O-S covered by Y-O-S (Fig. 2c). Hence, the higher the Y/Zr ratio, the higher the mass fraction of Y in the inclusions.

The TEM images of typical inclusions in 5Y3Zr and 11Y2Zr alloys with sizes smaller than 0.5 μm are shown in Fig. 3. Figure 3(a) illustrates the ellipsoidal inclusion. The components are similar to the micron-sized inclusions in 5Y3Zr alloy. Figure 3(b) is a compound inclusion containing Y and Zr. The inclusion shape in 11Y2Zr alloy is relatively regular. Similar to the morphology observed in the SEM, a submicron-sized spherical inclusion with Y is shown in Fig. 3(c). Moreover, the EDS (Fig. 3d) shows that Zr is not a component of this inclusion, which has the size of approximately 0.4 μm (Fig. 3d). These small size inclusions are difficult to remove

Table 2 Statistics of inclusions in the steel ingots

Nos.	$d_{A(i)} \geq 0.5$ μm			$d_{A(i)} < 0.5$ μm		
	$\bar{d}_V$, μm	N_V, $10^{14}/m^3$	f_V, %	$\bar{d}_V$, μm	N_V, $10^{16}/m^3$	f_V, %
1Y2Zr	1.79	1.51	0.04573	0.164	4.71	0.0110
5Y3Zr	1.30	2.58	0.02991	0.163	4.49	0.0102
11Y2Zr	1.32	2.51	0.03018	0.173	3.84	0.0105

Fig. 2 SEM images and compositions of inclusions in (a) 1Y2Zr, (b) 5Y3Zr, and (c and d) 11Y2Zr ingots
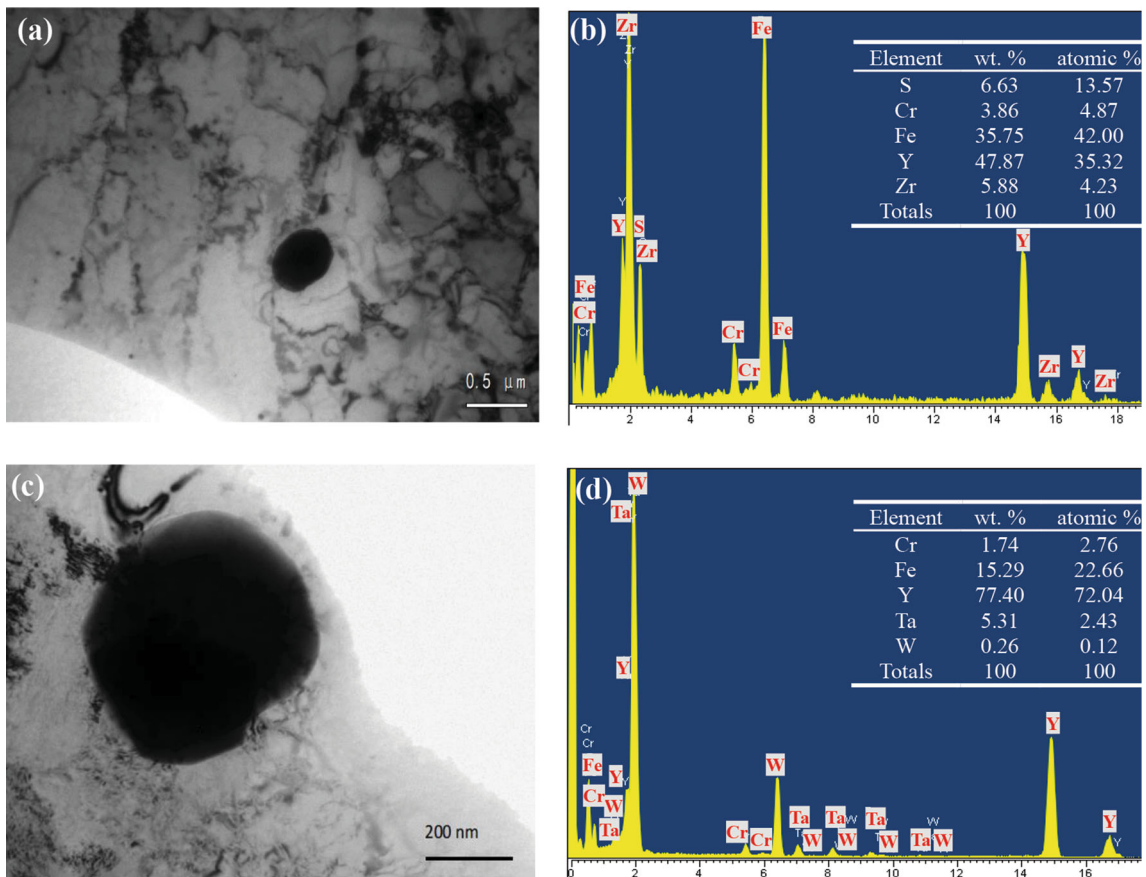
Fig. 3 TEM images and compositions of inclusions with sizes less than 0.5 μm
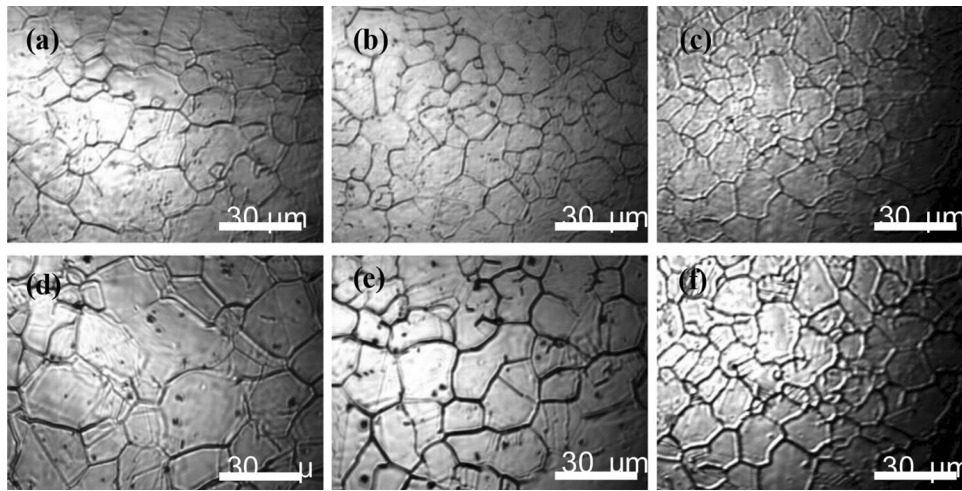
Fig. 4 CSLM results of (a and d) 1Y2Zr, (b and e) 5Y3Zr, and (c and f) 11Y2Zr alloy at 1323 K: initial moment (a-c) and 10 min (d-f)

during the melting process, and their metallurgical functions are gradually being valued by several researchers (Ref 27-29). These functions may play a good role in precipitation strengthening using carbides.

3.2 Effect of Particles on the Austenite Grain Size

The growth process of the austenite at 1323 K is shown in Fig. 4. Figure 4(a) and (d) illustrates a noticeable growth trend (i.e., 13.2 μm → 17.6 μm) of 1Y2Zr alloy. However, the trends in 5Y3Zr alloy (9.1 μm → 9.4 μm) and 11Y2Zr alloy (9.3 μm → 9.5 μm) were not evident. A large number of inclusions (black spots in Fig. 4) can be observed at the grain boundary of the steels. To control the austenite grain size, solidification structure refinement has been previously studied by using various deoxidation products in steels, such as TiN, TiO_X, MgO, ZrO_2, and Ce_2O_3 (Ref 28-30). The reason of the fine austenite grain is that the small micron-sized oxide inclusions can not only provide nucleation sites for acicular ferrite, but they also play a role in pinning the austenite grain boundaries based on the Zener pinning force. The mean austenite grain size, $\overline{D}_A$, is plotted against the Zener pinning force, Z_P, which is expressed as follows: (Ref 30)

$$Z_P = 3\sigma V f_V / \overline{d}_V,$$

where σ is the grain boundary energy (6×10^{-7} J/mm^2) and V is the molar volume of Fe (7×10^3 mm^3/mol).

Based on the data provided in Table 2, when only inclusions with sizes greater than 0.5 μm are considered, the Z_P can be represented as 205.4, 227.9, and 229.0 J/mol, respectively. When the inclusions smaller than 0.5 μm are also considered, the values are 284.0, 311.8, and 315.7 J/mol. S. Morioka and H. Suito reported that the grain size of austenite decreases with the increase in Zener pinning force in an unstable state. This result is consistent with the grain size in Fig. 4. In addition, the Y and Zr atoms in the solid solution may also restrict the growth of the austenite grains.

To determine the inclusion types at the grain boundary, an SEM was employed. Figure 5(a), (b), and (c) shows a large number of white second-phase particles at the grain boundary.

As illustrated in the figures, the particle size of 1Y2Zr alloy was the largest, whereas that of 5Y3Zr and 11Y2Zr alloys is smaller. The EDS of the inclusion (Fig. 5d, e, and f) demonstrated that the complex particle was a mixture of Y-Zr-O-S. In the results of section 3.1, the inclusions in 1Y2Zr alloy were mainly Y-Zr-O-S with MnS. However, no inclusions with MnS were found in 5Y3Zr and 11Y2Zr alloys. The inclusions can refine the microstructure owing to their pinning effect, and the reefing effect shows the Zener relation.

### 3.3 Microstructure and Precipitates

The detailed microstructural investigations were conducted using the OM and SEM. As shown in Fig. 6(a)-(c), the microstructures were tempered martensite, and the Vickers harnesses of the alloys were 265, 273, and 269 HV. The average prior austenite grain sizes measured using a linear intercept method are 14.5, 13.5, and 13.4 μm for 1Y2Zr, 5Y3Zr, and 11Y2Zr alloys, respectively, which are much smaller than the grain size of CLAM steels (20–30 μm) (Ref 31). Figure 6(d)-(i) shows the SEM micrographs of normalized steels with high magnification. Furthermore, the lath and prior austenite grain boundaries are decorated with $M_{23}C_6$ precipitates, and a few MC carbides are randomly distributed in the matrix, which has been observed in other ferritic/martensitic steels (Ref 7-14). The carbides are finer in 5Y2Zr samples with lower Y/Zr ratio than in other samples.

3.4 Tensile Test

3.4.1 Tensile Properties at RT. The objectives of the CLAM steel project (Ref 31), with tensile strength (TS) of 650 MPa and yield strength (YS) 550 Ma at RT, are listed in Table 3. As presented in the table, all the three steels can meet the objective of CLAM steel, particularly the TS and YS of 5Y3Zr alloy reaching 743.5 and 638.7 MPa, respectively. Compared with other RAFM steels, EUROFER97 (Europe), 9Cr2WVTa1.5Y (USA), ARAA (South Korea), and the optimized 0.22-CLAM steel (China), the performance of these three steels regarding strength and toughness is also excellent. Meanwhile, the tensile properties of the Y-Zr-infused steels are
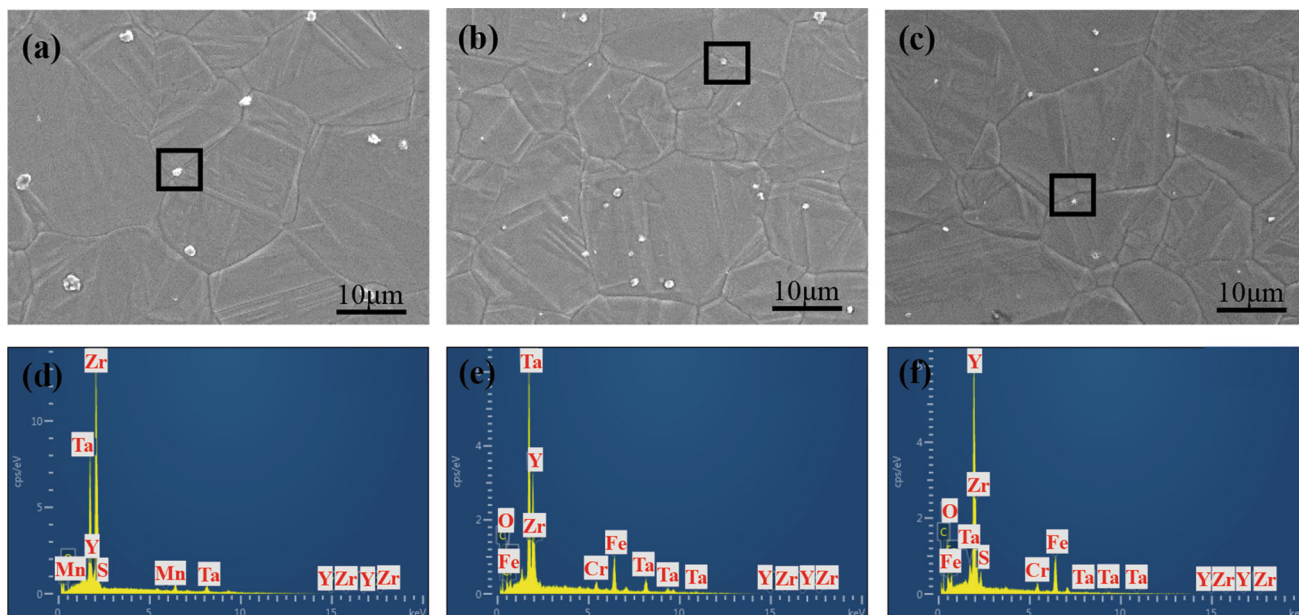
Fig. 5 SEM and EDS spectrum of inclusions observed in the experiment using the CSLM: (a and d) 1Y2Zr, (b and e) 5Y3Zr, and (c and f) 11Y2Zr alloy
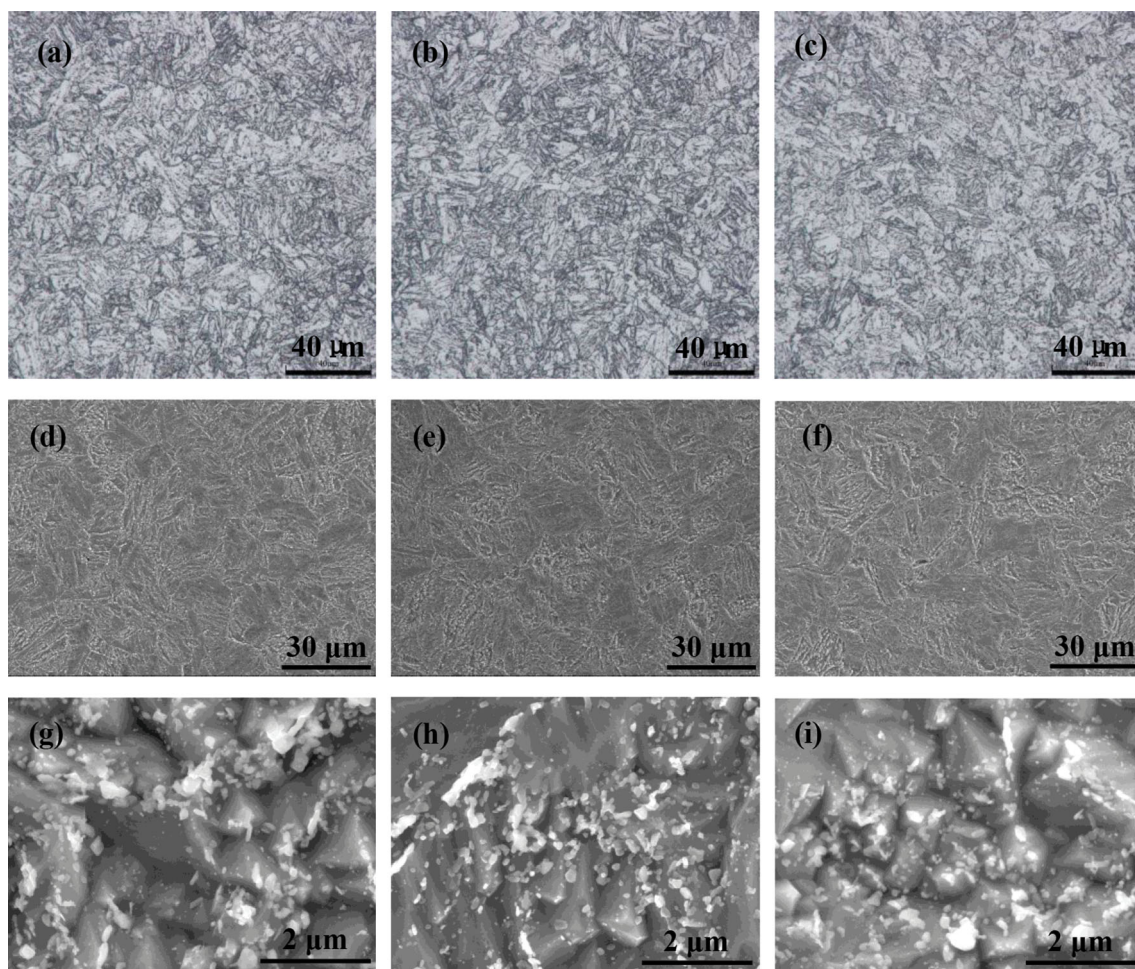
Fig. 6 OM and SEM images of the normalized and tempered steels: (a, d, and g) 1Y2Zr specimen, (b, e, and h) 5Y3Zr specimen, and (c, f, and g) 11Y2Zr specimen

Table 3 Tensile properties of steels

Specimens	σ, MPa	$\sigma_{0.2}$, MPa	δ, %	Specimens	σ, MPa	$\sigma_{0.2}$, MPa	δ, %
1Y2Zr	684.6	573.7	23.6	EUROFER97 (Ref 12)	650	540	22.5
5Y3Zr	743.5	638.7	25.2	9Cr2WVTa0.15Y (Ref 14)	627	483	21.0
11Y2Zr	697.9	591.7	26.4	0.22Si-CLAM (Ref 24)	675	540	23.5
Goal of CLAM (Ref 23)	650	550	…	ARAA (Ref 12)	…	525	21.5
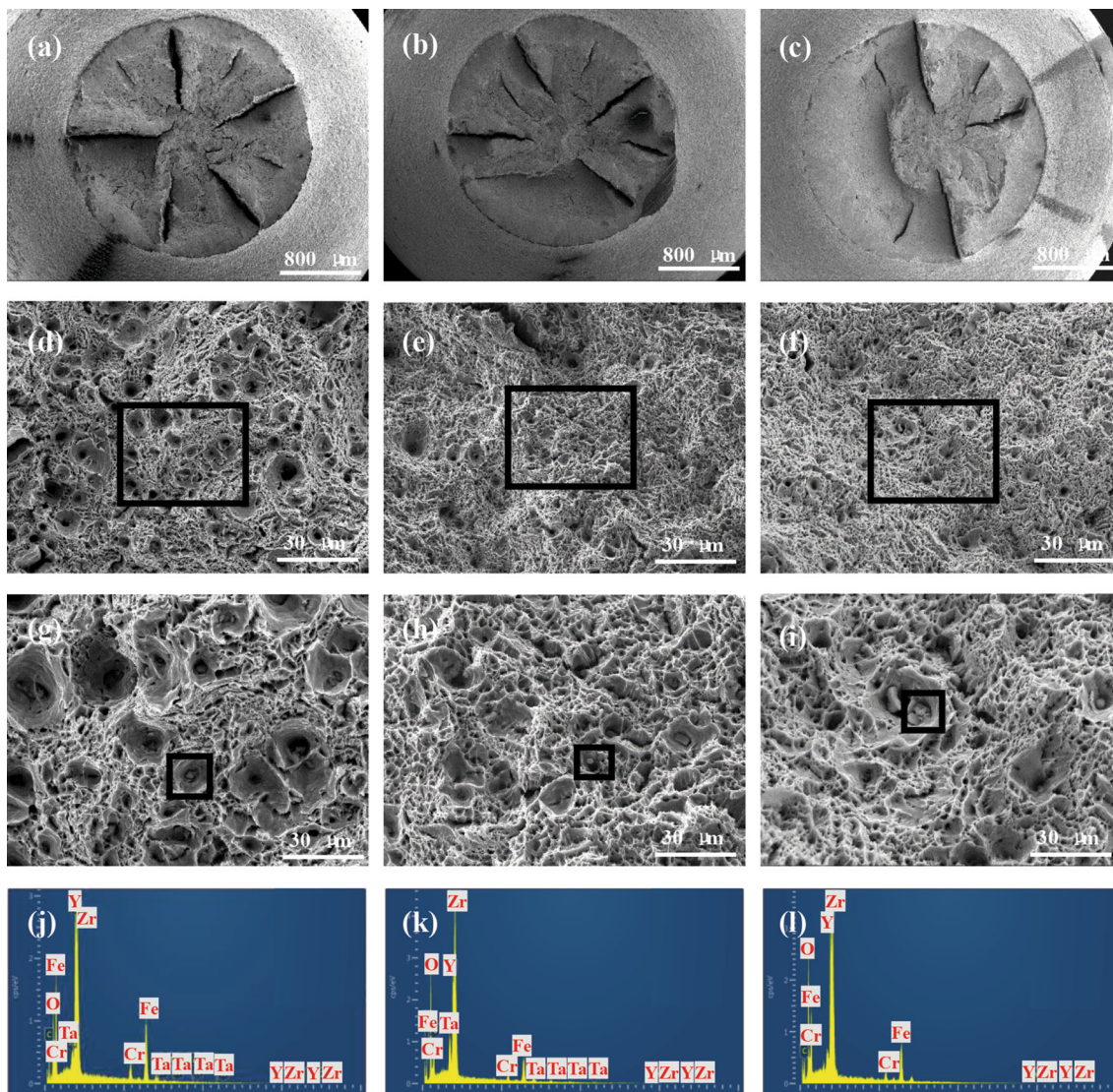
Fig. 7 Fracture surfaces of the steels: macroscopic (a, b, and c) and microscopic (e, f, and g) fracture morphologies and the corresponding EDS spectra (g, h, and i)

strongly dependent on their Y/Zr ratio (Table 3). When the Y/Zr ratio is increased from 1/2 to 5/3, the YS also increases from 573.7 to 638.7 MPa, and the ultimate TS increased from 684.6 to 743.5 MPa. When the Y/Zr ratio is further increased to 11/2, the YS and ultimate TS reduce to 697.9 MPa and 591.7 MPa, respectively, which is also higher than that of 1# alloy. Moreover, the alloy with the highest elongation is 11Y22Zr.

The fracture morphology of the steel is shown in Fig. 7. The fractures are typical ductile fractures exhibiting fiber, radiation, and shear lip areas (Fig. 7a-c). The morphologies were similar in the specimens that had the same composition. The fiber area and radiation zone indicate the sites of slow crack propagation and rapid crack growth, respectively. For the three specimens, significant ductile dimpling fractures can be observed (Fig. 7d-f). Spiral bands were also observed in dimple walls and were generated by shear stress around the particles: more ductility and toughness were achieved when the dimples widened and deepened under tensile stress. These dimples are mainly equiaxial with the 1Y2Zr steel being larger. Several large dimples may widen to more than 10 μm. Meanwhile, the

dimple sizes of 5Y3Zr and 11Y2Zr steels were evidently more uniform and smaller, and the smallest dimple size belongs to the 5Y3Zr alloy. In addition, inclusions with a diameter size of 1–3 μm are observed in many holes.

Additional details of the inclusions in the dimple are shown at the upper right-hand side of Fig. 7(g)-(i). The inclusions in the holes of 11Y2Zr alloy are much larger than those of the 5Y3Zr alloy but are smaller than in the 1Y2Zr alloy. This phenomenon is the main reason why the 11Y2Zr alloy has the smallest grain size, but its mechanical properties are worse compared with the 5Y3Zr alloy. According to the EDS analysis of the samples shown in Fig. 7(j)-(l), the inclusions of 11Y2Zr alloy comprised elemental Fe, Cr, Y, Zr, C, and O, whereas Fe, Cr, Y, Zr, C, O, and Ta are the components of the 5Y3Zr steel samples. Moreover, the inclusions of 1Y2Zr steel were mainly Fe, Cr, Y, Zr, C, O, Ta, and W. Assuming that these inclusions all contain elemental C and O, owing to the detection difficulty through EDS, the inclusions in the steels were regarded as compound with carbides and oxides, which is similar to the result obtained by Z. M. Shi (Ref 17) et al. Such inclusions play an important role in the dispersion strengthening of steels.
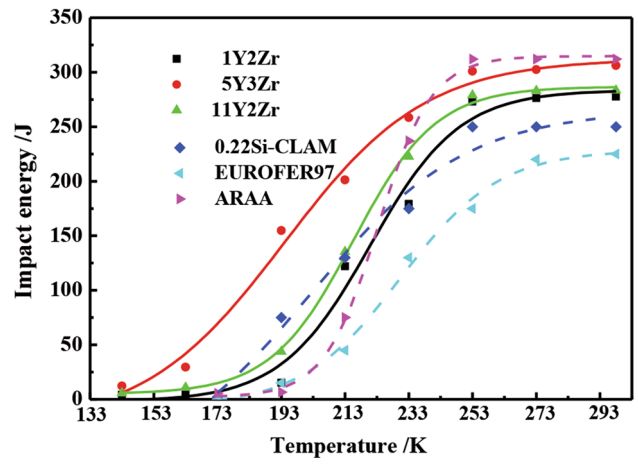
Fig. 9 Effect of the Y/Zr ratio on the variation of impact energy of the RAFM steels with test temperatures. The data for 0.22Si-CLAM (Ref 9), EUROFER97 (Ref 12), and ARAA (Ref 12) are provided for comparison
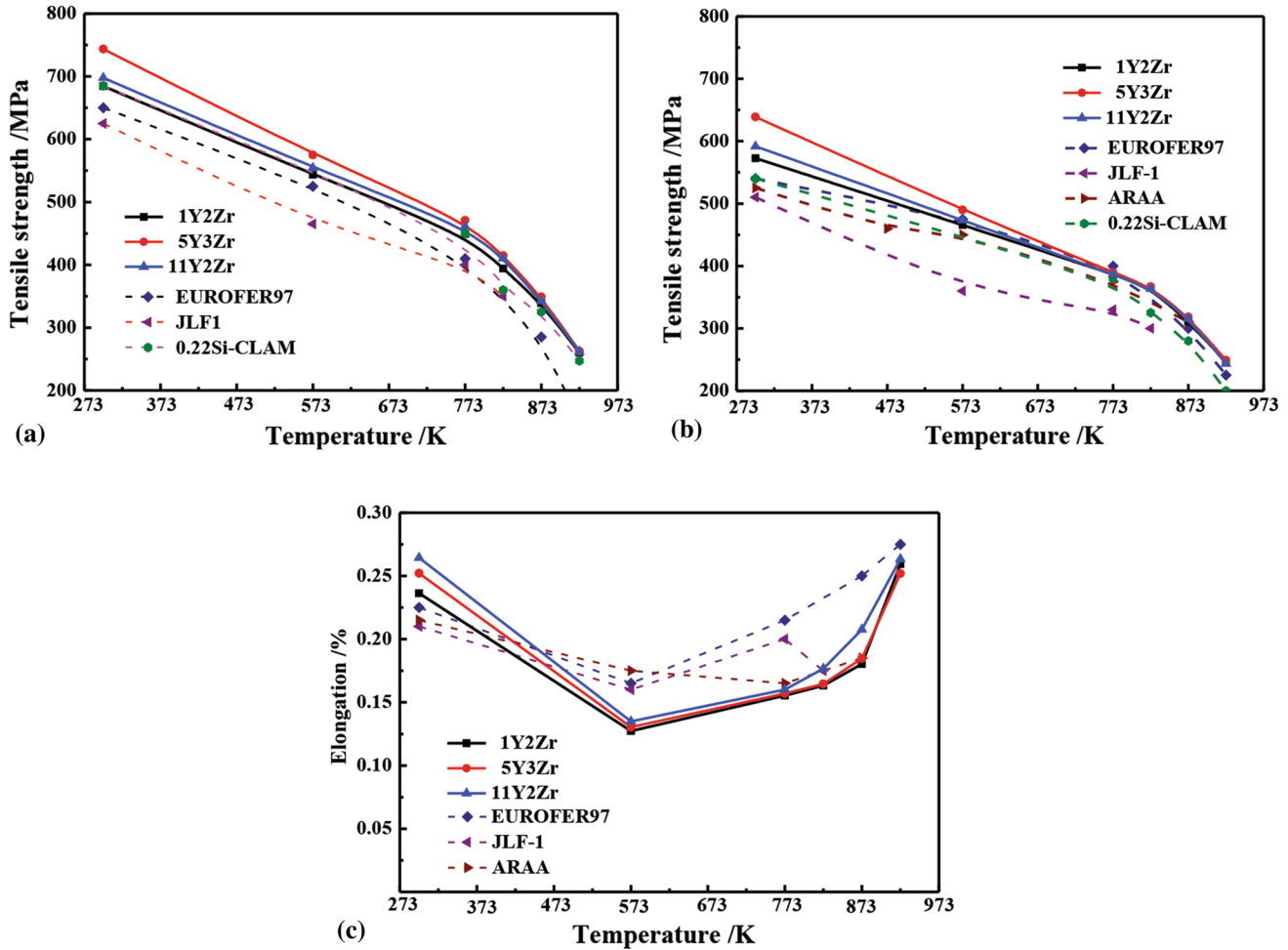
Fig. 8 Tensile properties of the steels at various test temperatures: (a) TS, (b) YS, and (c) elongation. The data for 0.22Si-CLAM (Ref 9), JLF-1 (Ref 33), EUROFER97 (Ref 12), and ARAA (Ref 12) are provided for comparison

Table 4 USE and impact transition temperatures obtained from the instrumented Charpy impact test of the investigated samples

Sample	1Y2Zr	5Y3Zr	11Y2Zr	ARAA (Ref 12)	0.22Si-CLAM (Ref 9)	EURFER97 (Ref 12)
DBTT (K)	220.8	194.0	215.6	223.3	202.3	230.4
USE (J)	277.6	306.2	283.4	312	250	225

3.4.2 Tensile Properties at High Temperature. With the aim of evaluating the effects of the Y/Zr ratio on high-temperature tensile properties, the tensile tests were performed on the 1Y2Zr, 5Y3Zr, and 11Y2Zr alloys at 573, 773, 823, 873, and 923 K. Figure 8(a)-(c) shows the TS, YS, and elongation of the steels at various test temperatures. As illustrated in the figures, the TS and YS of the three steels decreased with increasing test temperature. As the temperature increased, the elongation partially reduced and then increased. The inflection point was 573 K, as reported in other RAFM steels (Ref 7-14). Thus, the higher the Y/Zr ratio, the longer the elongation. A similar result is also achieved with other steels with Y and Zr (Ref 32). With the increase of the Y/Zr ratio from 1/2 to 11/2, the high-temperature tensile properties of the three specimens have similar trend changes at the same temperature: partially rising and then dropping. Although the mechanical performance of 1Y2Zr alloy was the lowest among the samples, its TS matched with those of JLF-1 (Ref 33) and EUROFER97 (Ref 12). Evidently, all the YS of the three steels is higher than that of JLF-1 (Ref 33), EURO-FER97 (Ref 12), ARAA, and the optimized 0.22Si-CLAM (Ref 9). This result is a product of the following factors: (i) fine prior austenitic grain size and (ii) introduction of submicron-sized inclusions.

3.5 Charpy Impact Test

The Charpy impact transition curves of the samples with different Y/Zr ratios are presented in Fig. 9. The transition curves were drawn by fitting the "Boltzmann" function [following the procedure in (Ref 34)] within the average values of the Charpy impact energy versus the test temperature (Fig. 9). The impact energy variation with temperature can be treated as two distinct regimes. In the temperature range of 253–298 K, it is called the upper shelf regime. As listed in Table 4, the upper shelf energy (USE) was found to partially rise and then reduce with the increase in the Y/Zr ratio. The maximum value belongs to 5Y3Zr alloy. As presented in Fig. 9 and Table 4, the USE of these three samples was higher than CLAM and EURFER97, but lower than that of ARAA, which had a Zr content of 0.02%. This result indicates that the addition of Zr is beneficial for the improvement of impact performance. For the test temperatures lower than 253 K, a steady decline in impact energy was observed (Fig. 9), and this energy decline is referred to as the transition temperature regime. The transition temperature regime is common in ferritic steels with body-centered cubic structures, similar to the investigated steel with tempered martensitic structure. The ductile-to-brittle transition temperature (DBTT) has been determined from the impact transition curves (Table 4). The presence of fine prior austenitic grain size and fine inclusions would be attributed to the decrease in the DBTT.

4. Conclusion

In the current work, three RAFM steels with different Y/Zr ratios were prepared to evaluate the effect of the Y/Zr ratio on the inclusions, microstructures, tensile properties, and impact toughness. The following conclusions were drawn from this work:

1. Generating inclusions containing Y-Zr-O becomes easy, which coincides with the results of the first principle calculation.
2. The statistical results show that most of the inclusions were smaller than 3 μm, and the proportion of inclusions smaller than 3 μm was more than 97% in every sample. The density of submicron-sized inclusions reached the reported density in 9Cr-ODS steel.
3. The prior austenite grain sizes decrease in direct correlation with the increase in the Y/Zr ratio. The micron-sized inclusions can refine the microstructure owing to their pinning effect, and the reefing effect shows the Zener relation.
4. The TS increases with the addition of Y and Zr at RT owing to both the refinement of prior austenite grain size and the fine submicron-sized inclusions. Hence, the smaller the grain size and the finer the inclusions, the better the mechanical properties of the steel.
5. Impact toughness is improved and the DBTT decreases when the Y/Zr ratio increases to 5/3. However, the toughness significantly decreases when the Y/Zr ratio reaches 11/2 owing to inclusion coarsening.

References

1. L.Y. Zhang, L.M. Yu, Y.C. Liu, C.X. Liu, H.J. Li, and J.F. Wu, Influence of Zr Addition on the Microstructures and Mechanical Properties of 14Cr ODS Steels, *Mater. Sci. Eng. A*, 2017, **695**, p 66–73
2. N. Baluc, D.S. Gelles, S. Jitsukawa, A. Kimura, R.L. Klueh, G.R. Odette, B. van der Schaaf, and J.N. Yu, Status of Reduced Activation Ferritic/Martensitic Steel Development, *J. Nucl. Mater.*, 2007, **367–370**, p 33–41
3. H. Fu, T. Nagasaka, T. Muroga, W.H. Guan, S.H. Nogami, A. Hasegawa, and H. Serizawa, Weldability of 9Cr-ODS and JLF-1 Steels for Dissimilar Joining with Hot Isostatic Pressing and Electron Beam Welding, *Plasma Fusion Res.*, 2017, **10**, p 1–4

4. F. Abe, Precipitate Design for Creep Strengthening of 9% Cr Tempered Martensitic Steel for Ultra-Supercritical Power Plants, *Sci. Technol. Adv. Mater.*, 2008, **9**, p 1–15

5. R. Mythili, S. Raju, G. Paneerselvam, T. Jayakumar, and E.R. Kumar, Effect of Alloy Content on Microstructure and Microchemistry of Phases During Short Term Thermal Exposure of 9Cr-W-Ta-0.1C Reduced Activation Ferritic/Martensitic (RAFM) Steels, *Bull. Mater. Sci.*, 2014, **37**, p 1453–1460

6. R. Ravikirana and S. Mythili, Influence of Tungsten and Tantalum Content on Evolution of Secondary Phases in 9Cr RAFM Steels: An Experimental and Computational Study, *Metall. Mater. Trans. A*, 2017, **48**, p 1–12

7. H.K. Kim, J.W. Lee, J. Moon, ChH Lee, and H.U. Hong, Effects of Ti and Ta Addition on Microstructure Stability and Tensile Properties of Reduced Activation Ferritic/Martensitic Steel for Nuclear Fusion Reactors, *J. Nucl. Mater.*, 2018, **500**, p 327–336

8. Q. Huang, C. Li, Y. Li, M. Chen, M. Zhang, L. Peng, Z. Zhu, Y. Song, and S. Gao, Progress in Development of China Low Activation Martensitic Steel for Fusion Application, *J. Nucl. Mater.*, 2007, **367–370**, p 142–146

9. S. Chen and L. Rong, Effect of Silicon on the Microstructure and Mechanical Properties of Reduced Activation Ferritic/Martensitic Steel, *J. Nucl. Mater.*, 2015, **459**, p 13–19

10. C.H. Lee, J.Y. Park, W.K. Seol, W.K. Seol, J. Moon, T.H. Lee, N.H. Kang, and H.C. Kim, Microstructure and Tensile and Charpy Impact Properties of Reduced Activation Ferritic–Martensitic Steel with Ti, *Fusion Eng. Des.*, 2017, **124**, p 953–957

11. G. Filacchioni, E. Casagrande, U. De Angelis, G. De Santis, D. Ferrara, and L. Pilloni, Tensile and Impact Behaviour of BATMAN II, Steels, Ti-Bearing Reduced Activation Martensitic Alloys, *J. Nucl. Mater.*, 1999, **271–272**, p 445–449

12. Y.B. Chun, S.H. Kang, D.W. Lee, S. Cho, Y.H. Jeong, A. Zywczak, and C.K. Rhee, Development of Zr-Containing Advanced Reduced-Activation Alloy (ARAA) as Structural Material for Fusion Reactors, *Fusion Eng. Des.*, 2016, **109–111**, p 629–633

13. Y.F. Li, Q.Y. Huang, Y.C. Wu, Y.N. Zheng, Y. Zuo, and ShY Zhu, Effects of Addition of Yttrium on Properties and Microstructure for China Low Activation Martensitic (CLAM) Steel, *Fusion Eng. Des.*, 2007, **82**, p 2683–2688

14. W. Yan, P. Hu, W. Wang, L.J. Zhao, Y.Y. Shan, and K. Yang, Effect of Yttrium on Mechanical Properties of 9Cr-2WVTa Low Active Martensite Steel, *Chin. J. Nucl. Sci. Eng.*, 2009, **29**, p 50–55

15. R. Chinnappan, Thermodynamic stability of oxide phases of Fe-Cr Based ODS Steels via Quantum Mechanical Calculations, *Procedia Eng.*, 2014, **86**, p 788–798

16. H. Xu, Z. Lu, D. Wang, and ChM Liu, Microstructure Refinement and Strengthening Mechanisms of a 9Cr Oxide Dispersion Strengthened Steel by Zirconium Addition, *Nucl. Eng. Technol.*, 2017, **49**, p 178–188

17. Z. Shi and F. Han, The Microstructure and Mechanical Properties of Micro-Scale Y_2O_3 Strengthened 9Cr Steel Fabricated by Vacuum Casting, *Mater. Des.*, 2015, **66**, p 304–308

18. D.P. Zhan, G.X. Qiu, Z.H. Jiang, and H.S. Zhang, Effect of Yttrium and Titanium on Inclusions and the Mechanical Properties of 9Cr RAFM Steel Fabricated by Vacuum Melting, *Steel Res. Int.*, 2017, **88**, p 1700159

19. J. Isselin, R. Kasada, and A. Kimura, Corrosion Behaviour of 16%Cr–4%Al and 16%Cr ODS Ferritic Steels Under Different Metallurgical Conditions in a Supercritical Water Environment, *Corros. Sci.*, 2010, **52**, p 3266–3270

20. A. Yabuuchi, M. Maekawa, and A. Kawasuso, Influence of Oversized Elements (Hf, Zr, Ti and Nb) on the Thermal Stability of Vacancies in Type 316L Stainless Steels, *J. Nucl. Mater.*, 2012, **430**, p 190–193

21. D. Murali, B.K. Panigrahi, M.C. Valsakumar, S. Chandra, C.S. Sundar, and B. Raj, The Role of Minor Alloying Elements on the Stability and Dispersion of Yttria Nanoclusters in Nanostructured Ferritic Alloys: An Ab Initio Study, *J. Nucl. Mater.*, 2010, **403**, p 113–116

22. J.H. Lee, R. Kasada, A. Kimura, T. Okuda, M. Inoue, S. Ukai, S. Ohnuki, T. Fujisawa, and F. Abe, Influence of Alloy Composition and Temperature on Corrosion Behavior of ODS Ferritic Steels, *J. Nucl. Mater.*, 2011, **417**, p 1225–1228

23. A. Karasev and H. Suito, Analysis of Size Distributions of Primary Oxide Inclusions in Fe-10 Mass Pct Ni- M (M=Si, Ti, Al, Zr, and Ce) Alloy, *Metall. Mater. Trans. B*, 1999, **30**, p 259–270

24. ChH Wu, L.F. Sun, ChB Lai, ZhH Deng, Q.X. Fu, and ChQ Yuan, Effect of Rare Earth Treatment on Inclusion of E36 Slab for Shipbuilding, *Iron Steel Van. Tit*, 2016, **37**, p 139–146

25. Q.X. Sun, Y. Zhou, Q.F. Fang, R. Gao, T. Zhang, and X.P. Wang, Development of 9Cr-ODS Ferritic–Martensitic Steel Prepared by Chemical Reduction and Mechanical Milling, *J. Alloys Compd.*, 2014, **598**, p 243–247

26. Q.L. Yong, *Secondary Phases in Steels*, Metallurgical Industry Press, Beijing, 2006

27. J.H. Shim, Y.J. Suh, Y.W. Cho, J.D. Shim, J.S. Byun, and D.N. Lee, Ferrite Nucleation Potency of Non-metallic Inclusions in Medium Carbon Steels, *Acta Mater.*, 2001, **49**, p 2115–2122

28. A. Karasev and H. Suito, Analysis of size distributions of primary oxide inclusions in Fe-10 mass Pct Ni- M,(M=Si, Ti, Al, Zr, and Ce)alloy, *Metall. Mater. Trans. B*, 1999, **30**, p 259–270

29. S. Morioka and H. Suito, Effect of Oxide Particles on δ/γ Transformation and Austenite Grain Growth in Fe-0.05-0.30%C-1.0%Mn-1.0%Ni Alloy, *ISIJ Int.*, 2008, **48**, p 286–293

30. D. Weygand, Y. Bréchet, and J. Lépinoux, Zener Pinning and Grain Growth: A Two-Dimensional Vertex Computer Simulation, *Acta Mater.*, 1999, **47**, p 961–970

31. Z.Y. Zhong, H. Saka, T.H. Kim, E.A. Holm, Y.F. Han, X.S. Xie. The Structure and Properties of Low Activation Ferritic/Martensitic Steels, In *Materials Science Forum*. 2005, 1383–1386

32. Z.M. Wang, Z.C. Zhang, S. Qin, L. Mao, and Y.M. Li, Effects of Zr, Y and Ba-Ca Modifier on the Microstructure and Properties of 00Cr25Ni7Mo4N Steel, *Special Cast. Nonferrous Alloys*, 2011, **31**, p 113–256

33. Q.Y. Huang, C. Li, and Y. Li, R&D Status of China Low Activation Martensitic Steel, *Chin. J. Nucl. Sci. Eng.*, 2007, **27**, p 36–41

34. Q.M. Wan, R.S. Wang, G.G. Shu, and L.K. Weng, Analysis Method of Charpy V-notch Impact Data Before and After Electron Beam Welding Reconstitution, *Nucl. Eng. Des.*, 2011, **241**, p 459–463